

Heterogeneous deformation and texture development in halite polycrystals: comparison of different modeling approaches and experimental data

Ricardo A. Lebensohn^a, Paul R. Dawson^b, Hartmut M. Kern^c, Hans-Rudolf Wenk^{d,*}

^a*Instituto de Física Rosario (UNR-CONICET), 27 de Febrero 210 Bis, 2000 Rosario, Argentina*

^b*Sibley School of Mechanical and Aerospace Engineering, Cornell University, Ithaca, NY 14853, USA*

^c*Institut für Geowissenschaften, Universität D-24098 Kiel, Germany*

^d*Department of Earth and Planetary Science, University of California, Berkeley, CA 94720, USA*

Accepted 31 March 2003

Abstract

Modeling the plastic deformation and texture evolution in halite is challenging due to its high plastic anisotropy at the single crystal level and to the influence this exerts on the heterogeneity of deformation over halite polycrystals. Three different assumptions for averaging the single crystal responses over the polycrystal were used: a Taylor hypothesis, a self-consistent viscoplastic model, and a finite element methodology. The three modeling approaches employ the same single crystal relations, but construct the polycrystal response differently. The results are compared with experimental data for extension at two temperatures: 20 and 100 °C. These comparisons provide new insights of how the interplay of compatibility and local equilibrium affects the overall plastic behavior and the texture development in highly anisotropic polycrystalline materials. Neither formulation is able to completely simulate the texture development of halite polycrystals while, at the same time, giving sound predictions of microstructural evolution. Results obtained using the finite element methodology are promising, although they point to the need for greater resolution of the individual crystals to capture the full impact of deformation heterogeneities. © 2003 Elsevier B.V. All rights reserved.

Keywords: Halite deformation; Polycrystal plasticity; Texture development; Self-consistent model; Finite element model

1. Introduction and motivation

Halite (NaCl) occurs naturally as a single phase mineral with cubic crystal structure. Halite exhibits high ductility, as evidenced by tectonic formations such as salt domes in nature (e.g. Sannemann, 1968; Trush-eim, 1957, 1960), and by deformation experiments

(e.g. Heard, 1972; Kern and Braun, 1973; Skrotzki and Welch, 1983; Franssen and Spiers, 1990; Carter et al., 1993; Skrotzki et al., 1995). Associated with the large strain deformations are pronounced changes in crystallographic texture. Also observed in halite is a strong degree of plastic anisotropy at single crystal level (Carter and Heard, 1970; Skrotzki and Haasen, 1981; Guillope and Poirier, 1979), a behavior that is attributed to the sparseness of its slip systems. With relatively few slip systems available, the yield strength

* Corresponding author. Fax: +1-510-643-9980.

E-mail address: wenk@seismo.berkeley.edu (H.-R. Wenk).

is highly directional. Consequently, it is unusual for crystals within a polycrystal to experience closely similar deformations. This combination of high ductility, that enables large strains, and strong anisotropy, that encourages high variability of strain from crystal to crystal, makes the simulation of texture evolution in halite particularly challenging.

Taylor (1938) suggested that in modeling plastic deformations, straining could be partitioned equally among crystals undergoing a macroscopically uniform deformation. This “full constraints” (FC) hypothesis has been used extensively for single-phase polycrystals comprised of crystals with cubic symmetry and having many slip systems of comparable strength available (e.g. Van Houtte, 1982; Kocks et al., 1998). For this approach even to be viable, the individual crystals must each be able to accommodate an arbitrary deformation, requiring five independent slip systems. While the Taylor assumption is reasonable for materials comprised of crystals with many slip systems of comparable strength, using it in other situations can lead to prediction of excessively high stresses, incorrect texture components, or both. The modeling of halite is consistent with these trends. If only the primary (weakest) families of slip systems are allowed, there are too few to permit arbitrary deformations. If secondary (much stronger) slips are made available and the deformation over an aggregate is required to be uniform, the computed stress levels are too high and the predicted textures are in error (Siemes, 1974).

In contrast to the Taylor hypothesis, all crystals in a polycrystal can be required to exhibit identical stress given that their behavior is rate dependent at the slip system level. This is a variant of the original Sachs assumption for rate independent behavior in which the stresses in the crystals throughout an aggregate share a common direction. The equal stress hypothesis is most effective for polycrystals comprised of crystals with fewer than the five independent slip systems. It has also been used successfully in modeling the mechanical response of lower symmetry crystals that possess adequate numbers of independent slip systems, but whose slip systems display widely disparate strengths. Halite has been modeled with this assumption, with limited success. The principal drawback is that deformation often is concentrated too highly in a small number of crystals, leading to inaccurate texture predictions.

Several other approaches have been developed for modeling the heterogeneous deformation of highly anisotropic polycrystals. For example, Molinari et al. (1987) developed the viscoplastic self-consistent (VPSC) formulation for large strain deformation in which each grain was regarded as an inclusion embedded in a viscoplastic homogeneous equivalent medium (HEM) whose properties coincide with the average properties of the polycrystal. For face-centered cubic metals with a single family of $\{111\}\langle 110 \rangle$ slip systems, the VPSC theory predicts textures that are similar those given by the Taylor hypothesis. The VPSC model also has been applied to halite (Wenk et al., 1989). In this case, the Taylor theory and VPSC predict entirely different behaviors. The activities of slip systems differ substantially, which, in turn, result in different predicted textures. This difference is evident in Fig. 1, which compares Taylor and VPSC simulations in the form of inverse pole figures, for the case of 50% extension, uniform initial texture, and no strain-hardening.

The tangent VPSC formulation of Molinari et al. (1987) assumed the HEM to be isotropic. A more general formulation with an anisotropic HEM behavior was introduced by Lebensohn and Tomé (1993, 1994). This fully anisotropic tangent VPSC has been successfully applied to the prediction of plastic anisotropy and texture development of various metals (e.g. Tomé and Canova, 1998) and geologic materials (e.g. Wenk, 1999). In most cases, the VPSC simulations improves earlier predictions obtained with the Taylor model, giving texture components which are observed but not computed using the latter model, as well as providing better overall quantitative agreement with experiments. However, in the case of halite the VPSC and the Taylor texture predictions show essentially opposite texture trends. This extreme discrepancy between the two models has never been adequately explained.

In recent years, the self-consistent models for non-linear polycrystals have been subjected to several extensions and reinterpretations. In particular, it was shown that due to its linearization scheme, the tangent VPSC formulation, as originally conceived, approaches the rate-insensitive Sachs limit (Tomé and Canova, 1998). To overcome this limitation, the rate-sensitive self-consistent approach has been extended to consider an ad-hoc linearization of the HEM (Masson

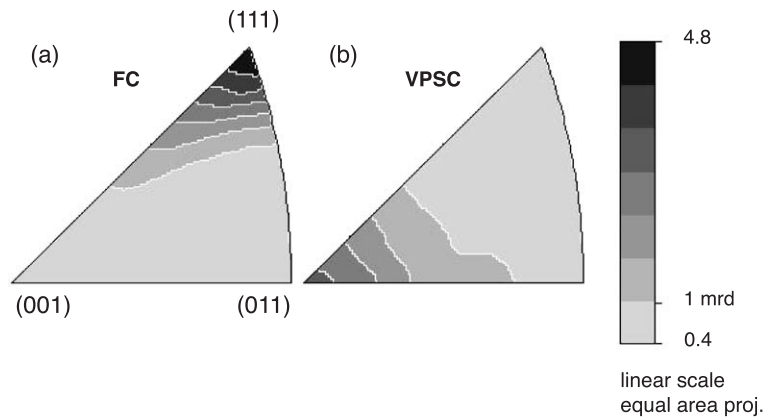


Fig. 1. Inverse pole figures of halite deformed 50% in extension, starting from random texture and with no strain hardening, predicted with (a) Taylor full constraint and (b) VPSC models (Wenk et al., 1989).

et al., 2000). In the present work, however, the modeling results required for comparison with the corresponding halite experiments remain largely within the range of validity of the tangent VPSC model. According to Ponte Castañeda (1991, 1996) the concept of an individual grain deforming homogeneously embedded in a HEM can be reinterpreted as the interaction between a phase of a perfectly disordered polycrystal, consisting of grains of the same orientation but different (i.e. random) neighborhoods, with the effective medium. In this case, the self-consistent model allows the calculation of statistical quantities associated with the deformation of a polycrystal with such random microstructure, particularly the mean value of the deformation in the phase, i.e. an average over grains with the same orientation and all possible environments.

Another modeling approach is to employ finite element methodologies to compute deformations of an aggregate of crystals. One example is the hybrid element polycrystal (HEP) approach reported by Beaudoin et al. (1995). Using the hybrid element approach, every grain can be discretized with a single element (Sarma and Dawson, 1996) or with many elements (Mika and Dawson, 1999). The boundary value problem resulting from the application of homogeneous macroscopic boundary conditions is solved to obtain the deformation of individual crystals. The HEP model has been applied to a number of one and two-phase metal alloys (aluminum, steel and titanium systems) to predict texture development and intracrystalline misorientations (Barton and Dawson, 2001).

In this paper, we reexamine the issue of predicting the evolution of texture in halite by comparing the results from Taylor, VPSC and HEP simulations. To establish a direct orientation-to-orientation comparison we use here the 1-site VPSC (Lebensohn and Tomé, 1993) and the one-element-per-grain HEP (Beaudoin et al., 1995). Newly obtained experimental data serve as a reference for comparison. Precise knowledge of the experimental conditions facilitates imposing the correct initial texture and boundary conditions in the simulations and assures consistency between measured stress–strain behavior and final textures. The intent of comparisons is to expose the influence of the deformation heterogeneity on the evolution of texture, and, in doing so, explain the reason for the wide discrepancy in the prior Taylor and VPSC predictions. In Section 2 we present new experimental data for extensional deformation of halite. In Section 3 we review and compare the assumptions underlying the Taylor, VPSC and HEP models, and report some details of the implementation of a HEP calculation for halite. In Section 4 we compare the local strain distribution, the stress–strain response and the texture development predicted with Taylor, VPSC and HEP models. Sections 5 and 6 contain discussion of results and conclusions, respectively.

2. Experiments

Texture evolution in halite has been examined by a number of investigators. Kern and Braun (1973)

deformed fine-grained halite in axial compression, plane strain and axial extension in a triaxial apparatus similar to the one described below. In all cases, substantial texture development was observed and reported as experimental pole figures. At the time quantitative texture analysis was not yet routinely available. Skrotzki and Welch (1983) extruded rock salt and other halogen compounds at a range of temperature and strain conditions, producing strong textures at very large strains as revealed by inverse pole figures. The extrusion textures display (111) and (100) fibers. At large strains, deformation was accompanied by dynamic recrystallization. Franssen and Spiers (1990) (and corrections by Franssen, 1996 and Skrotzki et al., 1996) deformed halite in simple shear and observed an asymmetric texture pattern similar to torsion textures in fcc metals (Canova et al., 1984; Hughes et al., 2000). Skrotzki et al. (1995, 1996) deformed halite in plane strain, pure shear and observed similar texture patterns as those described by Kern and Braun (1973). A complicating aspect for interpreting these experimental data is that the textural, mechanical and microstructural description is incomplete. Therefore, it seemed worthwhile to perform a series of new experiments, with well-defined starting material and a fairly complete characterization of the experimental conditions and the deformed material.

2.1. Experimental settings

Experiments were performed in a triaxial multi-anvil apparatus, obtaining quantitative mechanical data (stress–strain behavior). The microstructure of the samples was analyzed by optical microscopy on polished and etched surfaces. Pole figures and inverse pole figures shown in this paper and used for texture representation were recalculated from the orientation distribution function (ODF), based on three experimental, incomplete pole figures, measured by X-ray diffraction in reflection geometry, applying necessary defocusing and background corrections. The textures of some samples were additionally measured by SEM-EBSF. With the EBSF method, a flat sample surface was scanned in the automatic mode and the orientation distribution was reconstructed from about 1000 individual orientation measurements. Processing of texture data was done with BEARTEX (Wenk et al., 1998).

In this study, polycrystalline samples were prepared from granular rock salt with grain sizes < 0.4 mm by compaction in a steel matrix for several hours at a temperature of 120 °C and a confining pressure of 200 MPa to a nearly cubic shape with 5 cm edges. The residual porosity over the aggregate varied between 2.3% and 0.7%. Prior to loading, some of the samples were annealed at 650 °C for about 24 h. For comparison, typical microstructures of the compacted and annealed samples are shown in Fig. 2a and c, indicating that recrystallization did occur during annealing of the synthetic aggregates. The average grain size increased slightly during the annealing process, and the grains in the annealed samples were more uniform and did exhibit a more polygonal microstructure, with many triple junctions.

It was first established that the texture of the starting material was uniform (no preferred orientation) and that no texture was introduced during compaction. This is particularly important, because at the moderate strains reached in the experiments, the deformation textures were still quite weak. Fig. 3 shows (100) pole figures (incomplete and recalculated from the ODF) of the compacted and annealed samples. The observed intensity peaks that reach values higher than seven multiples of uniform (random) distribution (mrd) are essentially due to limited statistics. Therefore these fluctuations are not relevant, as far as the uniformity of the texture is concerned. Since single crystals of halite have a cubic cleavage, sample compaction could have conceivably introduced an artificial cube texture, but this was not observed.

The deformation experiments were carried out in extension mode ($\sigma_1 < \sigma_2 = \sigma_3$) (note that the major strain is compressive under these conditions), in a triaxial (multi-anvil) pressure apparatus (for details, see Kern, 1979). Graphite was sprayed on the end faces of the sample cube/prisms to minimize friction. Starting from hydrostatic conditions ($\sigma_1 = \sigma_2 = \sigma_3 = 50$ MPa) a deviatoric coaxial stress was obtained by increasing the principal stresses σ_2 and σ_3 continuously until a strain rate of about 10^{-5} /s was achieved. Afterwards the experiments were continued at constant strain rate. Strain ($\epsilon_1, \epsilon_2, \epsilon_3$) was determined from the measurement of the piston displacements, using two sensors on each prism side. Estimated precision of the displacement is about 10^{-2} mm. The applied principal stresses $\sigma_1, \sigma_2, \sigma_3$

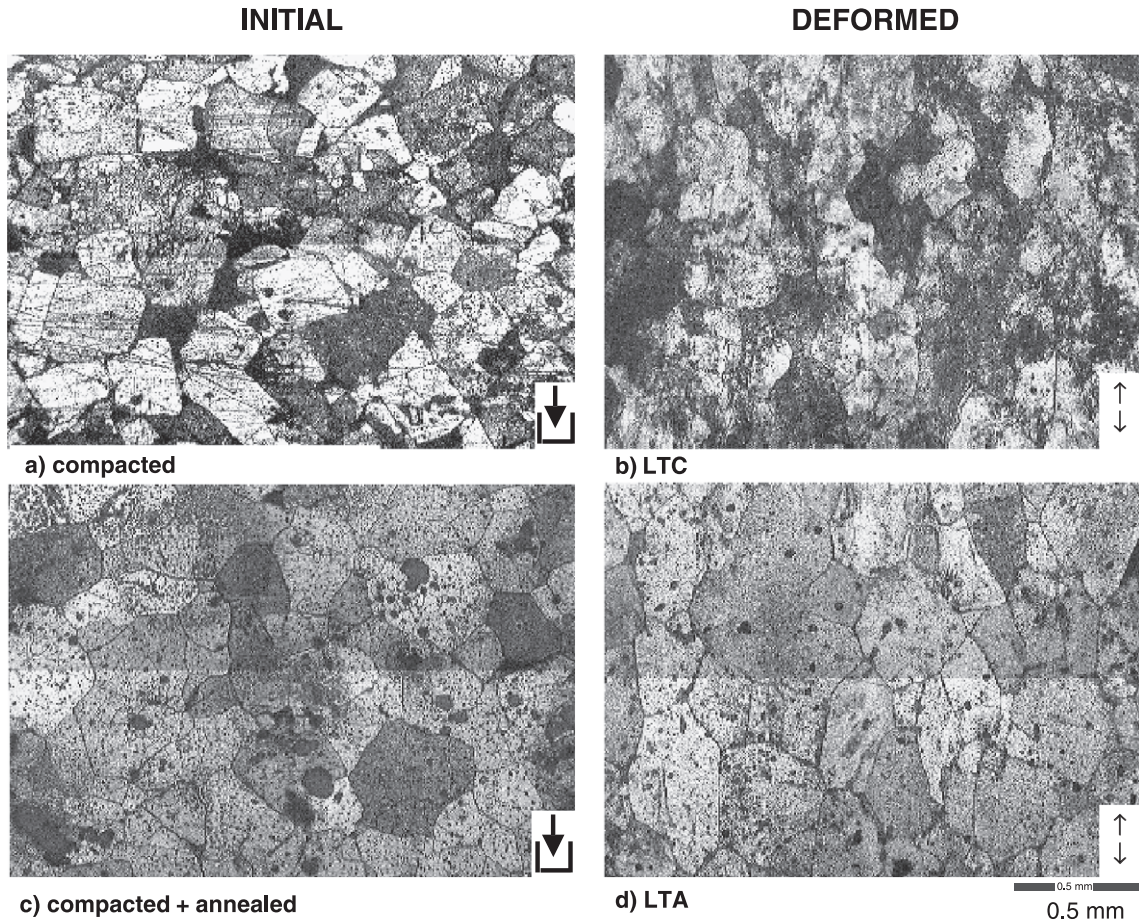


Fig. 2. Microstructures of (a,c) starting material (arrows indicate compaction direction) and (b,d) specimens deformed at room temperature (arrows indicate extension direction). Top: compacted only. Bottom: compacted and annealed.

were calculated from the measured forces and automatically corrected for deformation-related changes of the cross sections. The forces (loads) applied to the three pairs of faces with the three pairs of pistons were calibrated by means of a load cell. The estimated precision of the principal stresses is better than 2 MPa.

Three experiments were conducted under the following conditions: (a) at room temperature (20 °C), starting from the compacted state (LTC experiment); (b) at room temperature, starting from the annealed state (LTA experiment); and, (c) at higher temperature (100 °C), starting from the annealed state (HTA experiment). Experimental conditions and strain values for the specimens are listed in Table 1.

2.2. Stress–strain behavior

The stress–strain curves presented in Fig. 4 illustrate significant strain hardening in the samples deformed at room temperature. The maximal differential stress ($\sigma_{\max} = \sigma_3 - \sigma_1$) is about 66 MPa in the LTC sample and about 60 MPa in the LTA at final extensional strains of -15.5% and -16.6% , respectively. The stress–strain curves for the HTA sample under the same loading conditions exhibit only moderate hardening and finally weak softening. The maximal differential stress is considerably lower than the corresponding room temperature experiment (LTA), reaching a value of about 36 MPa. The pronounced weakening is partially due to

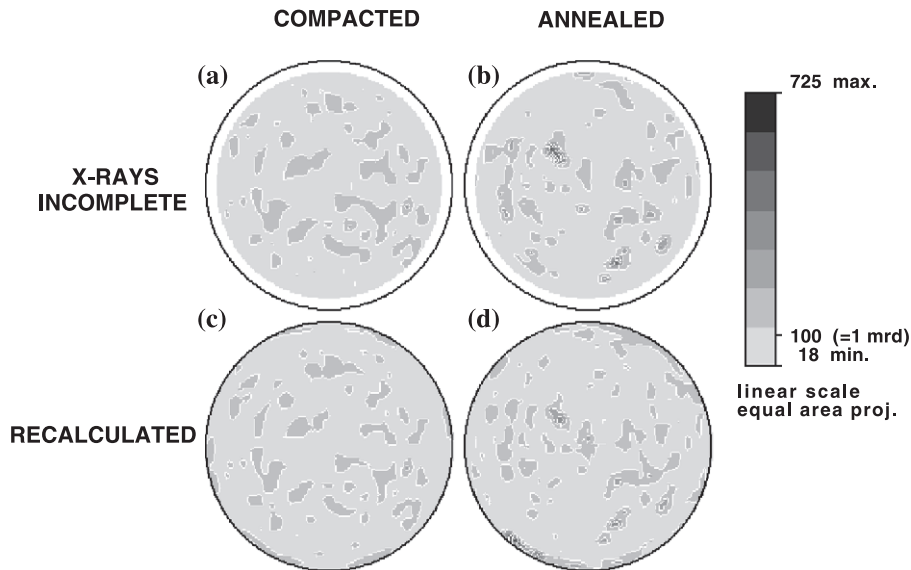


Fig. 3. (200) pole figures of the initial material. Top: Incomplete pole figures measured by X-ray diffraction. Bottom: Pole figures recalculated from the orientation distribution function. Equal area projection, linear contours.

reduced work-hardening (Carter and Heard, 1970; Skrotzki and Haasen, 1981), to texture development, and, conceivably, to effects of partial dynamic recrystallization.

2.3. Morphologic textures

Cylinders having a 20-mm diameter were cored from the roughly 5 cm cube-shaped deformed samples, parallel to the extension axes. A thick polished section cut normal to the extension (cylinder) axis was prepared from the central part for measurement of the texture. For microstructural investigations, a second thick polished section was cut parallel to the extension axis from an adjacent part of the specimen. For the microstructural analysis the polished surfaces were

carefully etched, ensuring a better visualization of the grain shapes. The grain contours were manually hand-drawn, digitised and ellipses were fitted automatically to those contours. Fig. 5 shows the quantified results of the shape fabrics parallel to the direction of deformation (compaction and extension, respectively) for the investigated samples in the initial and deformed states, respectively. The preferred 2D-orientation and the grain diameters are represented as rose diagrams (left) and solid bar histograms (center and right). The rose diagrams on the left display the frequency of long grain axes relative to the extension direction. The histograms in the center represent the percentage of area frequency corresponding to the lengths of the long axis of the grains and, those on the right, to the aspect ratio (length/width) of the

Table 1
Deformation conditions for the three experiments on halite polycrystals

Test	Starting material	Porosity (%)	T ($^{\circ}\text{C}$)	σ_1 (MPa)	σ_{max} (MPa)	Linear strain (%)		
						ϵ_1	ϵ_2	ϵ_3
LTC	compacted	0.7	20	50	66.1	–15.5	11.1	11.0
LTA	compacted + annealed	2.3	20	50	60.2	–16.6	12.3	12.0
HTA	compacted + annealed	0.74	100	50	34.2	–18.0	13.2	13.4

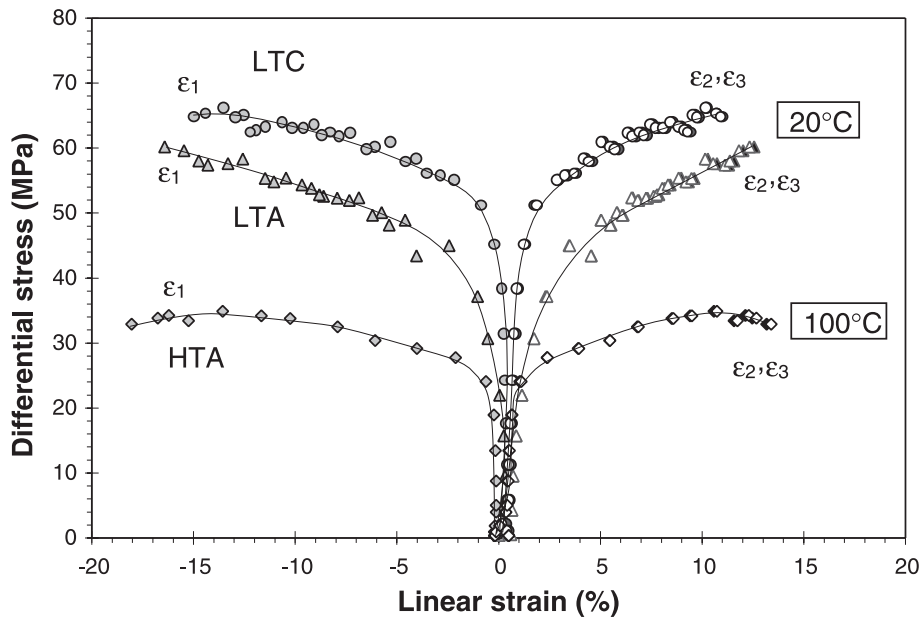


Fig. 4. Stress–strain curves of three halite specimens: room temperature (20 °C) starting from compacted material (LTC), room temperature, compacted + annealed (LTA) and high temperature, compacted + annealed (HTA), deformed in extension mode.

grains. The starting material shows only a weak orientation of the long axis perpendicular to the quasi-uniaxial compaction direction. Importantly, due to the annealing procedure, the average grain sizes increases from about 0.1 mm in the hot-pressed material to about 0.2 mm in the annealed specimen. Further, the grain shape distribution is more uniform for the annealed specimen. Polished and etched thin sections of the material deformed in extension reveal densely developed dislocation microstructures in heterogeneous domains, such as slip band patterns. Grain shapes tend to become elongated (ellipsoidal) in the deformed samples and a marked increase in the frequency of grains with their long axes oriented parallel to the extension direction is apparent. The distribution of grain size is somewhat broader in the deformed material in comparison to the initial distribution.

2.4. Crystallographic textures

Fig. 6 shows three inverse pole figures of the extension direction of the deformed samples (LTC, LTA and HTA) measured by X-rays and a fourth one measured by EBSD for the HTA sample. All inverse

pole figures display a bimodal distribution with texture components at (001) and (111). They differ, however, in the absolute intensity and in the relative intensity of the components.

Comparing the results for all three deformed samples we note that:

- (100) and (111) texture components appear at both 20 and 100 °C (both for the compacted and the annealed samples).
- At room temperature, the (111) component is more intense in the compacted sample (>4 mrd) than in the annealed sample (>2 mrd).
- Although the X-ray texture patterns are similar at 20 and 100 °C for the initially annealed samples, they are slightly stronger for 20 °C than for 100 °C even though the 100 °C samples were subjected to a larger strain (see Table 1).
- At 100 °C, the EBSD inverse pole figure shows a slightly weaker texture than the X-ray measurement. In addition, in the EBSD texture the (100) component dominates over the (111) component, while for the X-ray textures, the reverse is true. We believe that the X-ray results are more reliable because, with automated EBSD operation, some

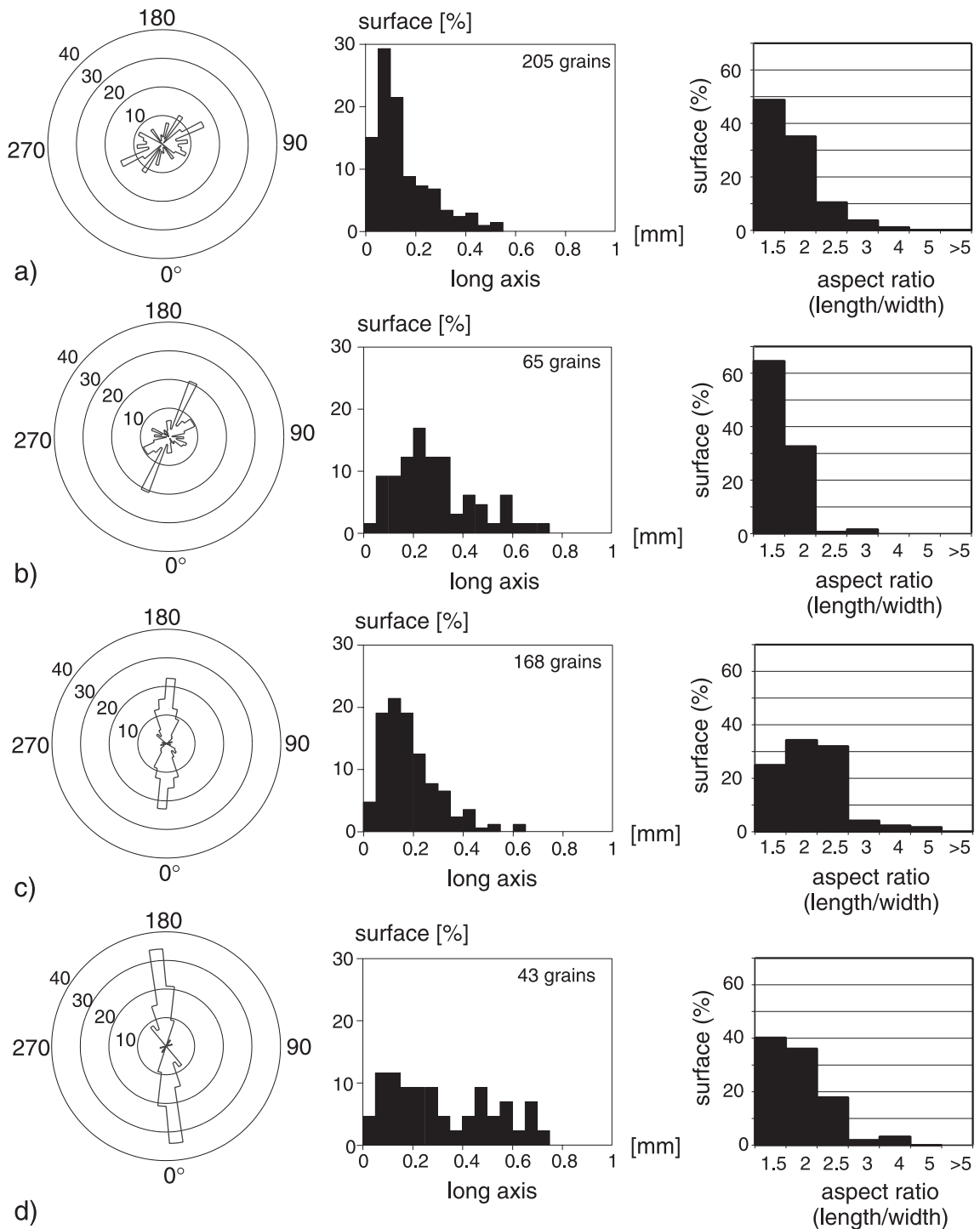


Fig. 5. Statistical information about shape preferred orientation (left side), grain size distribution (center) and grain shape distribution (right side) in initial and deformed halite aggregates. Frequency distributions refer to area percentages. (a) Initial compacted; (b) initial compacted + annealed; (c) LTC; (d) HTA.

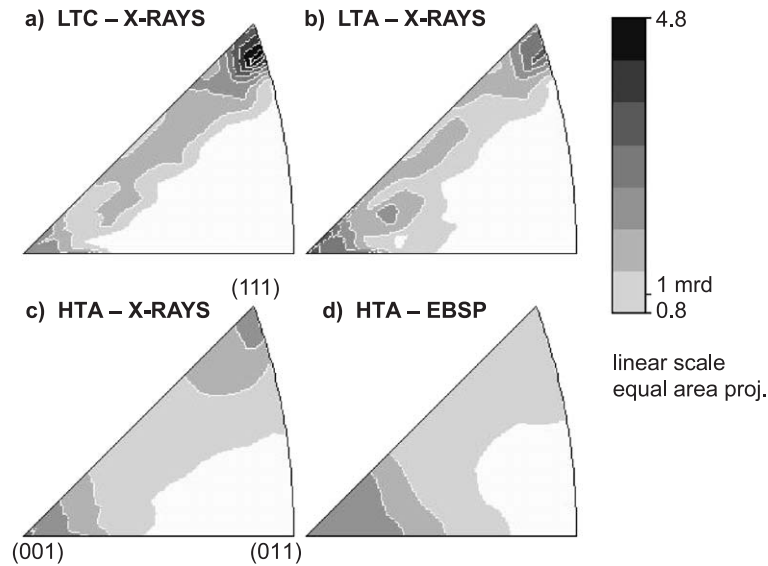


Fig. 6. Inverse pole figures of halite deformed in axial extension: (a) LTC sample, measured by X-rays; (b) LTA sample, X-rays; (c) HTA sample, X-rays; (d) HTA sample, measured by EBSP. Equal area projection, linear contours in mrd.

diffraction patterns were not indexed or were incorrectly indexed, producing apparent texture weakening. Moreover, there was an orientational bias of patterns that were indexed, leading to an emphasis of the (100) component.

The new texture results for axial extension are different than the extrusion experiments of Skrotzki and Welch (1983) which show, in non-recrystallized samples, only a (111) texture component. We attribute this to differences in deformation conditions. Skrotzki and Welch's extrusion strains were very large, and the applied strain-rates were many orders of magnitude larger than in our experiments (1 s^{-1} compared to 10^{-5} s^{-1}). The large strains are likely to cause heating that may be in excess of $70 \text{ }^\circ\text{C}$. In addition, there could be significant hardening of grains, such that after only moderate deformation all slip systems operate with similar ease. Both effects would promote a (111) texture. Details of the local deformation behavior are best evaluated at low strain rates and intermediate strains, where grain boundaries still remain more or less intact.

A microstructural survey ascertained that, at the time of the texture measurements, the material in the new experiments had not undergone substantial recrystallization. Secondary recrystallization may have

occurred at a later stage. It has been observed by many investigators that at large strains, and particularly in the presence of moisture, halite easily recrystallizes (e.g. Guillope and Poirier, 1979; Skrotzki and Welch, 1983; Skrotzki et al., 1995; Trimby et al., 2000). The previously mentioned extrusion experiments of Skrotzki and Welch (1983), for example, show the clear recrystallization feature of a strong (001) ("cube") texture. A (001) fiber component was also observed in extruded galena (PbS), which is isostructural with halite but deforms preferentially by $\{100\}\langle 011 \rangle$ slip (Skrotzki et al., 2000). In low temperature deformation of halite, crystals with (001) oriented perpendicular to the extension axis are plastically very weak because they are optimally oriented for $\{110\}\langle 110 \rangle$ slip. They have a Taylor factor that is more than five times lower than grains with (111) or (110) parallel to the extension axis (Wenk et al., 1989). These highly deformed grains are likely to recrystallize. Recrystallization nuclei will grow and then those orientations will dominate the texture (Wenk et al., 1997).

While dynamic (primary) recrystallization produces a cube texture, we also have observed secondary recrystallization in deformed samples stored for several months after the deformation experiment. Anom-

alous growth produced very large crystals, several millimeters in size, and almost in perfect cube orientation. However, at the time of texture measurements, done before the microstructural characterization shown in Fig. 2b and d, recrystallization was not significant and we can be confident that the (001) texture component observed in our samples is due to plastic deformation rather than to recrystallization.

3. Modeling

Polycrystal plasticity models are comprised of two basic parts: a set of crystal equations describing properties and orientations and a set of equations that link individual crystals together into a polycrystal. The latter set provides the means to combine the single crystal quantities to define the polycrystal response on the basis of physically motivated assumptions regarding grain interactions. Here we focus on the influence that these assumptions, as embodied by different modeling approaches, have on the predicted evolution of texture and microstructure. The single crystal equations are the same for all modelling approaches discussed and are presented in the next section. This is followed by a brief summary of the grain interaction equations associated with each of the various modeling approaches.

3.1. Single crystal equations

Interest here is on the evolution of microstructure and texture over large plastic deformation of crystals. Consequently, we neglect the elastic response and assume that all straining is plastic and occurs by means of crystallographic slip. It is essential to separate that part of the motion that is associated with deformation from that part that represents the rotation, as these are crucial to understanding the reorientation features of the material's structure. To that end, the kinematics associated with the crystal motion can be stated as

$$\text{grad } \mathbf{u} = \mathbf{L} = \mathbf{D} + \mathbf{W}, \quad (1)$$

where \mathbf{u} is the velocity, \mathbf{L} is the velocity gradient, and \mathbf{D} (deformation rate) and \mathbf{W} (spin) are its symmetric and skew symmetric parts, respectively. Slip is a

volume-preserving motion, which is imposed by requiring the divergence of velocity, or equivalently, the trace of the deformation rate, to vanish

$$\text{div}(\mathbf{u}) = \text{tr}(\mathbf{L}) = \text{tr}(\mathbf{D}) = 0. \quad (2)$$

Under the assumption of negligible elastic strains, the deformation rate is equal to the plastic deformation rate \mathbf{D}^p achieved by a linear combination of the slip on α slip systems

$$\mathbf{D}^p = \mathbf{D}^p = \sum_{\alpha} \dot{\gamma}^{(\alpha)} \mathbf{P}^{(\alpha)}. \quad (3)$$

Here, \mathbf{P} is the symmetric part of the dyadic product, $\mathbf{b} \otimes \mathbf{n}$, known as the Schmid tensor, $\dot{\gamma}^{(\alpha)}$ is the rate of shearing on the α system, and primes denote the deviatoric part of the respective variable. The skew part of the velocity gradient is a combination of the spin associated with slip and the spin of the crystal lattice

$$\mathbf{W} = \dot{\mathbf{R}}^* \cdot \mathbf{R}^{*\text{T}} + \mathbf{W}^p, \quad (4)$$

where

$$\mathbf{W}^p = \sum_{\alpha} \dot{\gamma}^{(\alpha)} \mathbf{Q}^{(\alpha)}. \quad (5)$$

$\mathbf{R}^{*\text{T}}$ is the rotation of the lattice frame with respect to a reference, and \mathbf{Q} is the skew part of the Schmid tensor. With the slip system shearing rates known, Eq. (4) provides an expression for evolving the lattice orientation in each crystal.

The constitutive relations at single crystal level are written assuming of rate-dependent behavior. This behavior is approximated with a power law relation between the resolved shear stress on the α system, $\tau^{(\alpha)}$, and the rate of shearing on that system, $\dot{\gamma}^{(\alpha)}$,

$$\tau^{(\alpha)} = \hat{\tau} \left(\frac{\dot{\gamma}^{(\alpha)}}{\dot{\gamma}_0} \right)^m, \quad (6)$$

where $\hat{\tau}$ is the slip system strength, $\dot{\gamma}_0$ is a reference rate of shearing (set to 1 s^{-1} for every calculation in this work), and m is the rate sensitivity parameter with rate independent limit $m \rightarrow 0$. At the crystal level, the resolved shear stress, $\tau^{(\alpha)}$, is the projection of crystal

deviatoric Cauchy stress, σ' , onto the slip system via the Schmid tensor

$$\tau^{(\alpha)} = \mathbf{P}^{(\alpha)} : \sigma' \quad (7)$$

Inverting Eq. (6) and combining the result with Eqs. (3) and (7) results in a relation between the deformation rate and crystal deviatoric stress

$$\mathbf{D}' = \left[\sum_{\alpha} \frac{\dot{\gamma}_0}{\hat{\tau}} \left| \frac{\tau^{(\alpha)}}{\hat{\tau}} \right|^{\frac{1}{m}-1} \mathbf{P}^{(\alpha)} \otimes \mathbf{P}^{(\alpha)} \right] : \sigma' = \mathbf{M}^c : \sigma' \quad (8)$$

where \mathbf{M}^c is the crystal compliance, also known as the secant modulus (Kocks et al., 1998).

Halite has cubic crystal structure, but, due to its ionic character, exhibits several low symmetry slip modes with different relative strengths. At low temperature, the mode (i.e. a family of crystallographically equivalent slip systems) with lowest strength has slip direction $\mathbf{b} = \langle 1\bar{1}0 \rangle$ and normal $\mathbf{n} = \{110\}$. This mode has six different slip systems (see Table 2).

Table 2

Slip systems of the different slip modes active in halite single crystals

Slip mode	Slip systems					
	\bar{n}		\bar{b}			
$\{110\}\langle 1\bar{1}0 \rangle$	1	1	0	1	-1	0
	-1	1	0	1	1	0
	1	0	1	1	0	-1
	1	0	-1	1	0	1
	0	1	1	0	1	-1
	0	1	-1	0	1	1
$\{100\}\langle 011 \rangle$	1	0	0	0	1	1
	1	0	0	0	1	-1
	0	1	0	1	0	1
	0	1	0	1	0	-1
	0	0	1	1	1	0
	0	0	1	1	-1	0
$\{111\}\langle 1\bar{1}0 \rangle$	1	1	1	1	-1	0
	1	1	1	1	0	-1
	1	1	1	0	1	-1
	-1	1	1	0	1	-1
	-1	1	1	1	0	1
	-1	1	1	1	1	0
	1	-1	1	0	1	1
	1	-1	1	1	0	-1
	1	-1	1	1	1	0
	-1	-1	1	0	1	1
	-1	-1	1	1	0	1
	-1	-1	1	1	-1	0

There are two stronger slip modes: one has slip direction $\mathbf{b} = \langle 011 \rangle$ and normal $\mathbf{n} = \{100\}$ (six different slip systems) while the other has slip direction $\mathbf{b} = \langle 1\bar{1}0 \rangle$ and normal $\mathbf{n} = \{111\}$ (12 slip different systems). Provided all the slip modes have the same slip direction, they are usually referred using just their slip plane. As Wenk et al. (1989) has pointed out, the lower strength $\{110\}$ mode alone does not endow a crystal with sufficient independent slip systems to accommodate an arbitrary deformation.

It is convenient in solving for the crystal stresses for a known deformation rate to initiate the iteration procedure from a vertex of the rate independent single crystal yield surface. The vertices for halite are given in the five dimensional deviatoric stress space using the Lequeu convention (Lequeu et al., 1987). Under this convention the five coordinates of the space are

$$\begin{aligned} s_1 &= \sqrt{2}(\sigma'_{22} - \sigma'_{11}); & s_2 &= \sqrt{\frac{3}{2}}\sigma'_{33}; \\ s_3 &= \sqrt{2}\sigma'_{23}; & s_4 &= \sqrt{2}\sigma'_{13}; & s_5 &= \sqrt{2}\sigma'_{12}. \end{aligned} \quad (9)$$

In general, the coordinates of the vertices are functions of the strengths of the different slip modes. In the particular case of halite with $\hat{\tau}^{\{110\}} < \hat{\tau}^{\{100\}} = \hat{\tau}^{\{111\}}$ there are 42 irreducible vertices whose coordinates were computed using the algorithm of Tomé and Kocks (1985) and are given in Table 3. This table shows that the first two coordinates of every vertex are function only of the strength of the weaker mode while the last three coordinates depend only on the strength of the stronger modes. This particular dependence reflects that fact that any combination of the weaker $\{110\}$ slip systems is unable to accommodate shear stress components in a system associated with the crystal cubic axes.

The slip system strengths evolve with deformation. The evolution of $\hat{\tau}$ follows a modified Voce form

$$\hat{\tau}^{\alpha} = \Theta \left[\frac{\tau_s - \hat{\tau}^{\alpha}}{\tau_s - \tau_0} \right] \sum_{\alpha} |\dot{\gamma}^{(\alpha)}| \quad (10)$$

in which Θ (initial hardening), τ_0 (initial strength) and τ_s (saturation strength) are material parameters.

Table 3

Coordinates (Lequeu convention) of the 42 irreducible vertices of a halite single crystal for $\tau_0^{\{110\}} < \tau_0^{\{100\}} = \tau_0^{\{111\}}$. $A = \sqrt{2}\tau_0^{\{110\}}$, $B = \sqrt{6}/3\tau_0^{\{110\}}$, $C = \tau_0^{\{100\}}$

	σ_1	σ_2	σ_3	σ_4	σ_5
1	-A	-B	0	0	2C
2	-A	-B	0	0	-2C
3	-A	-B	0	-2C	0
4	-A	-B	0	2C	0
5	-A	-B	C	C	C
6	-A	-B	-C	C	-C
7	-A	-B	-C	-C	C
8	-A	-B	C	-C	-C
9	A	B	C	C	C
10	A	B	-C	C	-C
11	A	B	-C	-C	C
12	A	B	C	-C	-C
13	-A	-B	-2C	0	0
14	-A	-B	2C	0	0
15	A	-B	0	0	2C
16	A	-B	0	0	-2C
17	A	-B	0	2C	0
18	A	-B	0	-2C	0
19	A	-B	C	C	C
20	A	-B	-C	C	-C
21	A	-B	-C	-C	C
22	A	-B	C	-C	-C
23	-A	B	C	C	C
24	-A	B	-C	C	-C
25	-A	B	-C	-C	C
26	-A	B	C	-C	-C
27	A	-B	2C	0	0
28	A	-B	-2C	0	0
29	0	-2B	0	0	2C
30	0	-2B	0	0	-2C
31	0	-2B	0	-2C	0
32	0	-2B	0	2C	0
33	0	-2B	C	C	C
34	0	-2B	-C	C	-C
35	0	-2B	-C	-C	C
36	0	-2B	C	-C	-C
37	0	2B	C	C	C
38	0	2B	-C	C	-C
39	0	2B	-C	-C	C
40	0	2B	C	-C	-C
41	0	-2B	-2C	0	0
42	0	-2B	2C	0	0

3.2. Crystal interaction equations

Crystals within an aggregate collectively bear the loads applied to them and exhibit deformation to differing degrees. Generally, the greater the degree of crystal anisotropy or the larger the differences in

strength between crystals, the greater the inhomogeneity of the deformation both within and among the crystals. A difficult task in constructing a model for polycrystals is to ascertain how to partition the net (macroscopic) straining among the participating crystals of an aggregate. Numerous models have been proposed; here we examine only three.

3.2.1. Extended Taylor assumption

Following the Taylor's assumption that all crystals exhibit the same strain (Taylor, 1938), the velocity gradient in every crystal is equated to the macroscopic velocity gradient:

$$\boldsymbol{\eta} = \langle \mathbf{L} \rangle = \mathbf{L}, \quad (11)$$

where $\boldsymbol{\eta}$ is the macroscopic velocity gradient and the MacCaulley brackets indicate the ensemble average. The average of the crystal stresses defines the macroscopic stress:

$$\boldsymbol{\Sigma}' = \langle \boldsymbol{\sigma}' \rangle. \quad (12)$$

Because every crystal must deform in an identical manner to the macroscopic average (Fig. 7, bottom left), each crystal must be capable of accommodating the average deformation regardless of its orientation. For highly anisotropic crystals, this implies that stronger slip systems will be more active than is actually the case.

3.2.2. Viscoplastic self-consistent

Using the VPSC approach, the average deformation rate within a crystal can be determined by considering the problem an inclusion embedded in an homogeneous effective medium (HEM) and determining the deviation in the crystal's stress and deformation rate from the interaction equation obtained from the Eshelby inclusion in a viscoplastic medium:

$$\mathbf{D} - \bar{\mathbf{D}} = -\tilde{\mathbf{M}} : \left(\boldsymbol{\sigma}' - \boldsymbol{\Sigma}' \right), \quad (13)$$

where

$$\tilde{\mathbf{M}} = (\mathbf{I} - \mathbf{S})^{-1} : \mathbf{S} : \mathbf{M}, \quad (14)$$

is the interaction tensor, \mathbf{S} is the viscoplastic Eshelby tensor, and \mathbf{M} is the tangent compliance of the HEM,

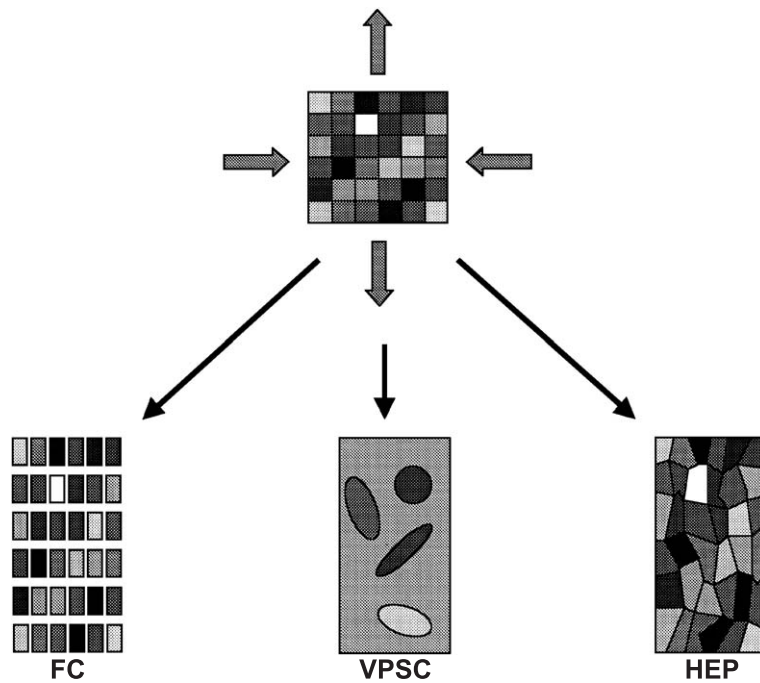


Fig. 7. Conceptual depiction of the modeling assumptions made with the Taylor (FC), self-consistent (VPSC), and finite element (HEP) models. A polycrystal is deformed as indicated by the arrows. Lattice orientation in each crystal is indicated by gray shades. Under the FC assumption, all crystals undergo the same average deformation regardless of their orientations and of their neighborhood. This independent behavior is shown schematically by the separation of the individual crystals. Under the VPSC assumption, crystals act as ellipsoids in an effective medium having uniform properties. The crystals deform differently based on the lattice orientation. All crystal with the same lattice orientation exhibit the same deformation. Under the HEP assumption, crystals deform differently but maintain compatibility. The deviation in deformation from the average depends both on lattice orientation and on the lattice orientations of neighboring crystals.

which is not known in advance, but rather must be determined by satisfying:

$$\bar{\mathbf{D}} = \langle \mathbf{D} \rangle, \quad (15)$$

and

$$\sum' = \langle \sigma \rangle. \quad (16)$$

Unlike the Taylor hypothesis, the straining in every crystal may be different than the macroscopic average. The interaction equation introduces the influence of neighboring crystals in an average sense over the complete polycrystal. Because the interaction equation is averaged over all crystals, the deviation in deformation rate from the average depends only on the crystal's own orientation and the overall texture (Fig. 7, bottom center).

3.2.3. Hybrid element polycrystal

Another possibility for determining the response of an aggregate of crystals is to resolve individual crystals with finite elements and solve for the velocity field based on the field equations using a finite element formulation. The hybrid finite element formulation of Beaudoin et al. (1995) is used for the solution procedure here. Equations for linear momentum balance, mass conservation and the crystal constitutive response are solved simultaneously to determine the motion and stress distribution in an aggregate of crystals. Hybrid formulations have two features that distinguish them from the more commonly employed displacement or velocity based formulations (Zienkiewicz and Taylor, 2000). First, there is mixed interpolation, meaning that the trial functions are defined for the motion and the stress. Second, residuals are formed using domain partitioning, which

in this case applies to partitioning of the body as individual crystals.

Beginning with balance of linear momentum, and neglecting body forces and inertia, a residual is formed on the tractions over all the crystal surfaces. After integration by parts, application of the Cauchy formula, and elimination of the $\text{div}\boldsymbol{\sigma}$ over the volume of elements by the choice of appropriate stress interpolation, this residual becomes

$$\sum_e \left[\int_{\Omega_e} \text{tr}[(\boldsymbol{\sigma}' - p\mathbf{I}) \cdot \text{grad}\Phi] d\Omega - \int_{\Gamma_t} \Phi \cdot \mathbf{t} d\Gamma \right] = 0, \quad (17)$$

where Ω_e are element volumes, $\boldsymbol{\sigma}'$ is the deviatoric Cauchy stress, p is the pressure, \mathbf{I} is the second order identity, \mathbf{t} is the applied surface traction, Γ_t is the portion of element surface with applied traction, tr is the trace operator, and Φ are vector weights. The second residual is from conservation of mass for an incompressible motion, as given in Eq. (2). In weak form with scalar weight φ , this becomes

$$\int_{\Omega} \varphi \text{tr}(\mathbf{D}) d\Omega = 0. \quad (18)$$

The crystal response shown in Eq. (8) provides the third residual required to obtain a solution of the boundary-value problem. This residual can be written with vector weights, Ψ , as

$$\int_{\Omega} \Psi \cdot (\mathbf{M}^c \cdot \boldsymbol{\sigma}) d\Omega = \int_{\Omega_e} \Psi \cdot \mathbf{D} d\Omega. \quad (19)$$

The constraints of Eqs. (17), (18) and (19) are sufficient to obtain a velocity solution to the boundary-value problem. The numerical solution begins by introducing trial functions for the velocity, pressure, and stress as

$$\mathbf{u} = [N^u]\{U\}, \quad p = [N^p]\{P\}, \quad \boldsymbol{\sigma}' = [N^\sigma]\{\beta\}. \quad (20)$$

Here, N^u , N^p and N^σ are the interpolation functions for the velocity, pressure and deviatoric stress, respectively. U , P , and β are the corresponding nodal values. The velocity trial functions provide continuous interpolation using trilinear functions. The pressure trial

functions are constant over elements and discontinuous. The stress trial functions are piecewise discontinuous and linear in the natural coordinates of the element, which ensures the invariant property of the element. The stress trial functions are chosen to satisfy $\text{div}\boldsymbol{\sigma}' = 0$ a priori at the element level. The stress will be divergence-free under the sum of the divergence-free deviatoric stress and the constant (and hence divergence-free) pressure. The stress now acts as the primary variable with the velocity serving the function of Lagrange multipliers. The hybrid formulation has proven to be very effective in aiding convergence in simulations where the properties change abruptly, as is the case at the interfaces of grains (elements). A simple Euler integration is employed to advance the geometry and microstructural state over a time increment once a converged solution is found.

In the present one-element–one-grain implementation of the HEP model, average values of the deformation rate and the stress in each crystal are calculated by interpolation at the centroid of each element. As with the VPSC model, the deformation rate in each crystal varies from the macroscopic average. Unlike the VPSC model, the deviation of the strain rate in a crystal depends on its local neighborhood. The deformation rate exhibited by a crystal thus depends not only on its own orientation and the texture as a whole, but also on that of its immediate neighbors in the HEP (Fig. 7, bottom right). Thus, two crystals within an aggregate having virtually identical orientations can experience quite different deformation histories.

4. Simulations

Simulations were performed to mimic the extension experiments using the three modeling approaches (Taylor, VPSC, and HEP). Identical single crystal slip system parameters were employed in all simulations so that the differences between simulations were a result of the grain interaction assumptions associated with the three approaches. Table 4 shows the initial threshold strengths and the hardening parameters (see also Eq. (10)) used to simulate the low and high temperature deformation experiments. The initial threshold strengths were taken from the Carter and Heard (1970) experiments on single crystals. The hardening parameters for 20 and 100 °C were ad-

Table 4

Initial threshold strengths, hardening parameters and anisotropy factors used to simulate the 20 and 100 °C halite deformation experiments

T [°C]	$\tau_0^{\{110\}}$ [MPa]	$\tau_0^{\{100\}} = \tau_0^{\{111\}}$ [MPa]	Θ_0 [MPa]	$\tau_s^{\{110\}}$ [MPa]	$\tau_s^{\{100\}} = \tau_s^{\{111\}}$ [MPa]	Anisotropy factor ($\tau_0^{\{110\}}/\tau_0^{\{111\}}$)
20	4.8	19.2	105	9.1	36.4	4.0
100	3.8	11.4	69.5	6.8	20.5	3.0

justed to obtain the best possible match between the HEP predictions and the experimental LTA and HTA stress–strain curves, respectively. For halite, the slip systems strengths differ appreciably for the various slip systems. In the simulations reported here, the stronger slip systems (i.e. the $\{100\}$ and $\{111\}$ systems) are four and three times stronger than the weaker $\{110\}$ system for 20 and 100 °C, respectively. The saturation values for the slip system strengths were chosen so that the ratio between the critical stresses of weaker and stronger slip systems remained constant as the deformations proceeded (i.e. homotetic hardening). For the rate-sensitivity of the slip systems strength, a value of $m=0.1$ was specified, as determined on single crystals by Carter and Heard (1970) and confirmed on polycrystals by Skrotzki et al. (1996).

A numerically built collection of 4096 orientations were chosen randomly from a uniform distribution with no symmetry constraint. The absence of an initial (nonuniform) texture is an important issue, given our interest in predictions for relatively low strains. In fact, after distributing the orientations into 5° ODF cells, filtering the discrete ODF with 10° Gaussians and calculating inverse pole figures using the BEAR-TEX package (Wenk et al., 1998), the orientation density of the initial inverse pole figure varied between 0.87 and 1.16 mrd (multiples of a random distribution).

The simulations were carried out imposing uniaxial tension along axis x_3 . For the Taylor and VPSC calculations, boundary conditions given by $\bar{D}_{33}=1$ for the strain rate in the tensile direction and $\Sigma'_1 = \Sigma'_2 = 0$ for the transverse stress components were assumed. Shear tractions were 0 on all surfaces. For the finite element simulations, the upper surface of a prismatic sample of lengths $L_1=L_2$ and $L_3=2L_1$ was submitted to a longitudinal velocity $u_3 = \bar{D}_{33}L_3$ while $u_3=0$ was imposed on the lower surface. On the lateral surface, the normal tractions were 0. On all surfaces, shear tractions arising from friction were

neglected. These boundary conditions are consistent with conditions of deformation and stress imposed on the Taylor and VPSC simulations. The HEP sample was regularly partitioned in each direction using a $16 \times 16 \times 16$ mesh (Fig. 8a). Each one of the initial 4096 orientations was randomly assigned to an element. In the Taylor and VPSC cases, the same 4096 orientations were used as initial texture but, unlike the HEP model, the Taylor and VPSC models do not utilize any information about neighborhood between grains.

This plastic anisotropy of halite single crystals is a challenge for the HEP model in several aspects. The most severe is associated with distortion of the element crystals with deformation. For each deformation increment, the coordinates of each node should be updated according to the corresponding local velocities. However, for highly anisotropic materials, the deformations vary strongly from one element to another. Within elements, there also exist spatial variations in the velocity gradient dictated in form by the interpolation functions and in magnitude by the differences in nodal velocities. Strong intra-element variations in velocity gradient lead to non-uniform element distortions that can be monitored with the Jacobian of the mapping of the element coordinates. As a simulation proceeds, some elements in the mesh can become heavily distorted, leading to deterioration of their numerical accuracy after relatively small amounts (a few percents) of overall strain of the polycrystal. One possible strategy to overcome this problem is to perform periodic remeshing operations. However, it is evident that remeshing can disrupt the one-to-one correspondence between element and grain. Consequently, to avoid either heavy mesh distortion or remeshing, the nodal coordinates were updated using a velocity field corresponding to a macroscopically homogeneous deformation. In the case of an initially untextured material pulled in uniaxial tension along axis x_3 of a prismatic sample of lengths L_1 , L_2 and L_3 , an isotropic velocity field is

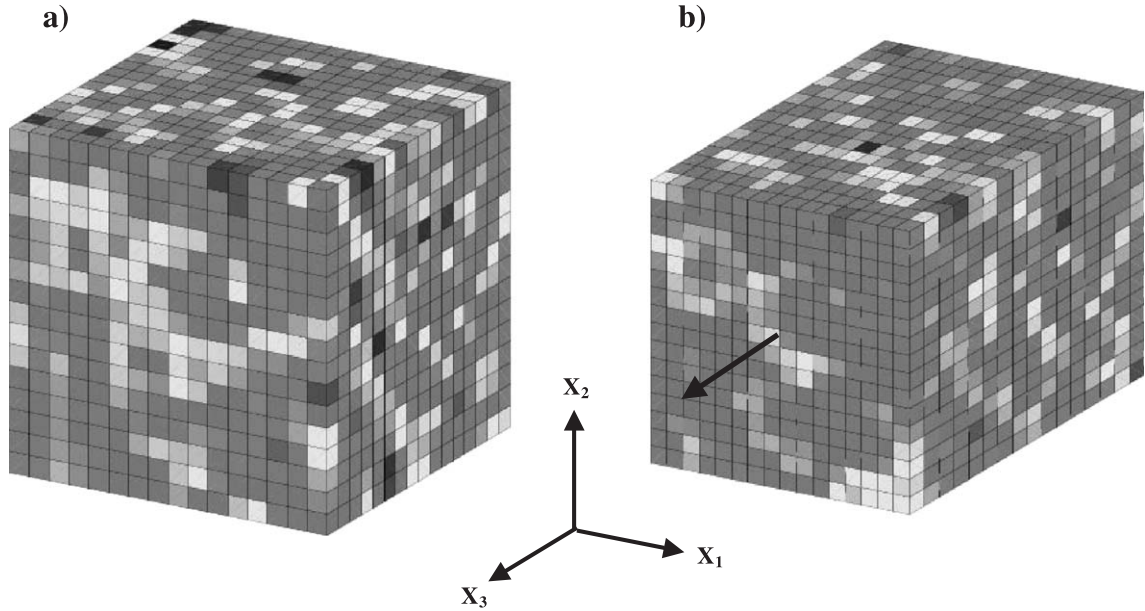


Fig. 8. Initial and deformed polycrystal after 30% strain, simulated with HEP model. Gray shades indicate levels of longitudinal strain-rate component.

adequate for this purpose and can be calculated at each deformation step (j) as:

$$u_i^{(j)}(\bar{x}) = \frac{x_i \dot{L}_i^{(j)}}{L_i^{(j)}} \quad (21)$$

where $\dot{L}_3^{(j)}$ can be updated as:

$$\dot{L}_3^{(j)} = \frac{\dot{L}_3^{(j-1)} L_3^{(j)}}{L_3^{(j-1)}} \quad (22)$$

and, if $L_1 = L_2$:

$$\dot{L}_1^{(j)} = \dot{L}_2^{(j)} = -\frac{L_1^{(j)} \dot{L}_3^{(j)}}{2L_3^{(j)}}. \quad (23)$$

Updating the nodal coordinates in this way gives a final polycrystal consisting of regular elongated prismatic grains, as shown in Fig. 8b. However, even applying this simplified scheme for grain (element) shape updating, we can still keep track of the actual grain shape that would result from using the local velocity gradients for that purpose. This allows us to use HEP to predict morphologic texture evolution (i.e. distributions of grain's principal axis orientations and aspect ratios), as discussed below. This method for

repairing distorted elements was used in the study of texture evolution in HCP polycrystals (Dawson et al., 1994). In that study, little difference was observed in computed textures between results obtained from simulations with and without mesh repair up to strain levels of about 10%.

5. Results

5.1. Comparisons between models

In what follows, we will compare the results obtained with VPSC and HEP formulation, (and also the Taylor model) for an aggregate represented by an identical set of initial orientations. However, it is worth emphasizing here that the microstructures considered under the assumptions underlying each formulation are indeed different. While in the HEP case we obtain the behavior of each grain surrounded by particular neighbors, in the VPSC case the deformation associated with each orientation represents an average of over grains with this orientation and all possible environments.

Fig. 9 shows the predicted loading curves in comparison to the experimental data for 20 (LTA

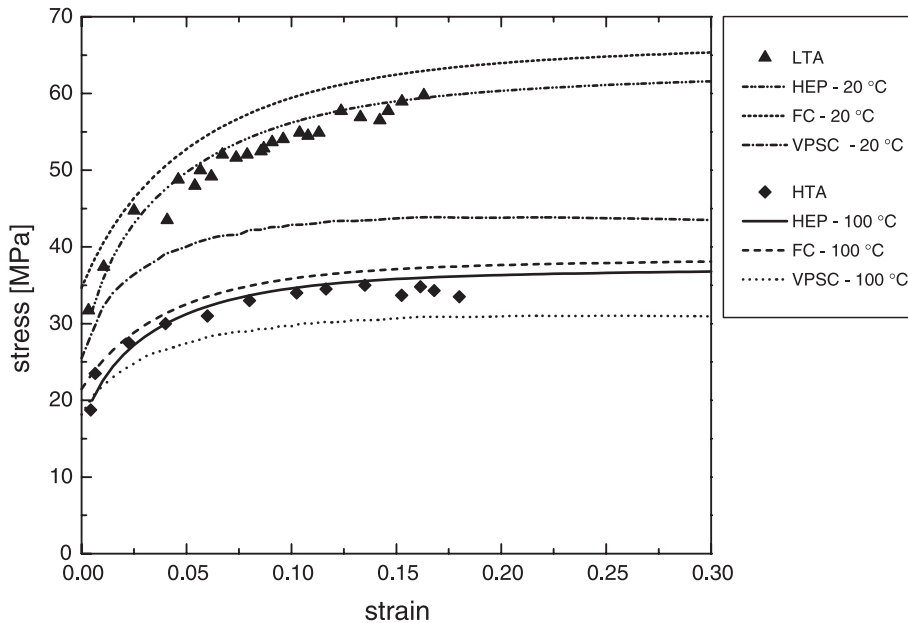


Fig. 9. Measured stress–strain points for LTA and HTA experiments and predicted loading curves at 20 and 100 °C using Taylor (FC), VPSC and HEP models.

case) and 100 °C (HTA case) test. Although the experiments conclude at around 15% strain, the simulations continue up to 30% strain. For the single set of input parameters, the Taylor FC model predicts the highest stress level throughout the test; the VPSC curve is substantially below the Taylor result; the curve predicted by HEP lies in-between, closer to Taylor than to the VPSC. The fact that HEP curves lie between Taylor and VPSC curves, but closer to Taylor, suggests that, although equilibrium is satisfied in the weak form as the chosen constraint, the fulfillment of spatial compatibility remains a strong constraint in the HEP model. This trend is systematically observed when other indicators are analyzed. In what follows, we will show some of these indicators for the 100 °C case.

Materials with strongly anisotropic single crystal behavior are expected to demonstrate a high level of strain heterogeneity over an aggregate of crystals. We can compare the heterogeneity predicted by the three modeling approaches by examining the distributions in strain rate components over the simulated aggregates of crystals. In Fig. 10 the strain rate component from the HEP and VPSC simulations are cross-plotted at the initial stage of each simulation. Fig. 10a shows

the major (extensional) diagonal component (the magnitudes of the two minor components are negative and approximately half of the major component) and Fig. 10b–d shows the off-diagonal components. The macroscopic prescribed values are indicated with large dotted symbols. If both models predicted the same local behavior the points would form a straight line at 45°. The horizontal and vertical spans reflect the local deviations from the macroscopic values for the HEP and the VPSC models, respectively.

The deviations predicted by the VPSC model are much larger than the ones obtained with the HEP formulation (i.e. in all cases, the vertical dispersions are higher than the horizontal ones). The spreads show a positive slope, but no strong correlation. In case of the off-diagonal components, for instance, the distribution is mainly located in the first and third quadrant rather than in the second and fourth. These slightly positive slopes can be explained in the following terms: while in the VPSC case the local strain-rate is only dictated by the orientation of each grain, in the HEP case the orientation but also the neighborhoods of a grain are relevant to determine its local behavior.

This becomes even more evident when plotting the component along the tensile direction of the local

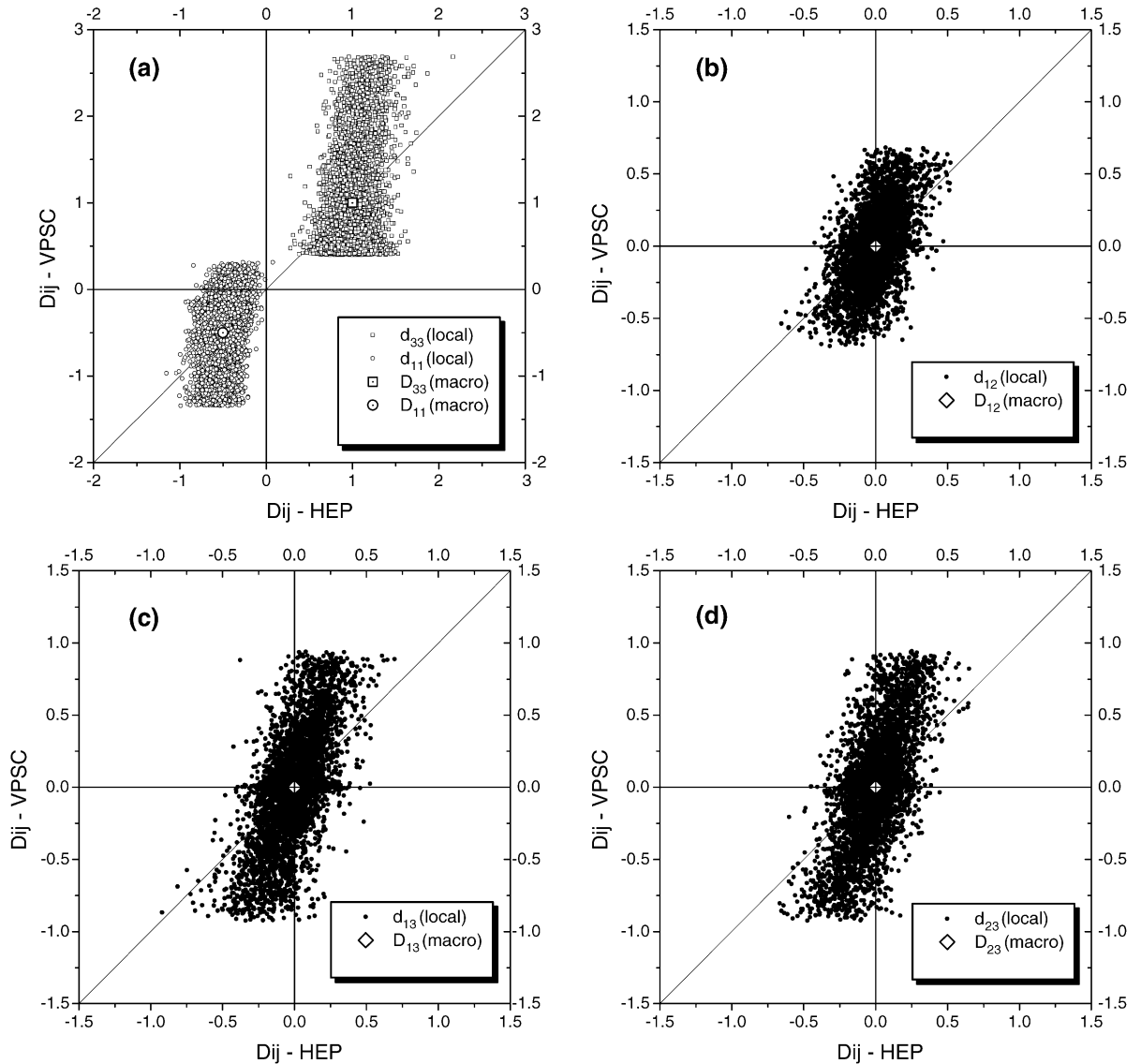


Fig. 10. Grain-by-grain comparison of (a) diagonal and (b–d) off-diagonal strain-rate components, predicted at the initial stage of each simulation, in the HTA case, with HEP (horizontal axes) and VPSC (vertical axes). Big symbols: applied macroscopic strain-rate components.

strain-rate (D_{33}) as a function of the Taylor factor of each orientation, defined as (Mecking et al., 1996):

$$M = \frac{\sigma'}{\tau_0^{(110)} \bar{D}} \quad (24)$$

where σ' is the deviatoric stress in the grain when it undergoes the macroscopically applied strain-rate \bar{D}

and $\tau_0^{(110)}$ is used as a reference hardness. Fig. 11 shows such plots for Taylor, VPSC and HEP at the initial stage of each simulation. In the Taylor case, the points obviously lie on a horizontal line, indicating that the predicted strain rates are independent of the orientation of the grains. In contrast, VPSC shows a strong dependence of the local behavior with the orientation, i.e. favorable orientations (with

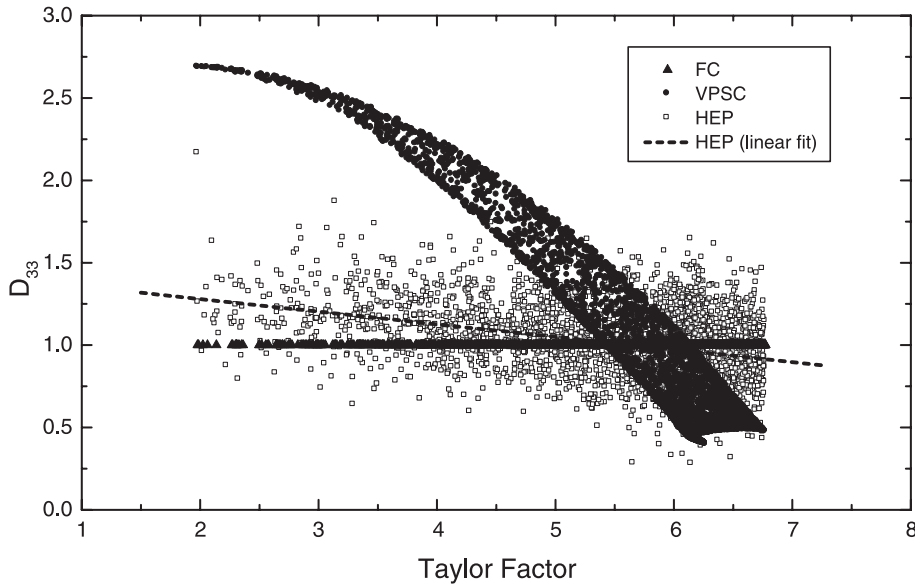


Fig. 11. Tensile component of the local strain-rate as a function of the Taylor factor for Taylor, VPSC and HEP models at the initial stage of each simulation in the HTA case. Straight line: linear regression of HEP points.

a low Taylor factor) deform more than twice as fast as the average. In fact, the VPSC points form a narrow cloud, i.e. grains with the same Taylor factor may undergo slightly different deformation. This small variance is a consequence of our choice of a single parameter like the Taylor factor to represent a crystal orientation relative to the tensile axis, which strictly depends on two angles. On the other hand, the HEP results differ substantially from both Taylor and VPSC: the points form a band that shows an important dispersion for orientations of identical Taylor factor and gives evidence of a strong influence of the local neighborhood of a grain on its behavior. When a linear fit is performed on the HEP data, a regression line with a slight negative slope is obtained. This means that, in the HEP case, the grain orientation, among other factors, still plays a role in determining the local deformation. The substantial differences between the VPSC and the HEP results at local level, displayed in Figs. 10 and 11, indicate that two models predict very different behaviors for the highly anisotropic halite polycrystals.

Two additional indicators of the differences between the modeling approaches are the relative activ-

ity of the slip modes and the average number of active slip systems per grain. The relative activity of slip mode (m) is defined as:

$$\text{act}^{(m)} = \left\langle \frac{\sum_{\alpha=1}^{S^{(m)}} \dot{\gamma}^{(\alpha)}}{\sum_{\alpha=1}^S \dot{\gamma}^{(\alpha)}} \right\rangle \quad (25)$$

where the summation in the denominator runs over the whole set of active slip systems while the one in the numerator runs over the slip systems of mode (m). To compute the average number of active slip systems per grain, a given slip system is considered to be active if its strain rate exceeds a threshold shear-rate of 20% of the most active slip system. Fig. 12a and b shows the plots of the relative activity and numbers of active slip system over the course of the simulated deformation, respectively. In the Taylor case, the activity of the hard modes is higher than the activity of the soft $\{110\}$ slip. This result (already discussed by Wenk et al., 1989) is a direct consequence of the Taylor assump-

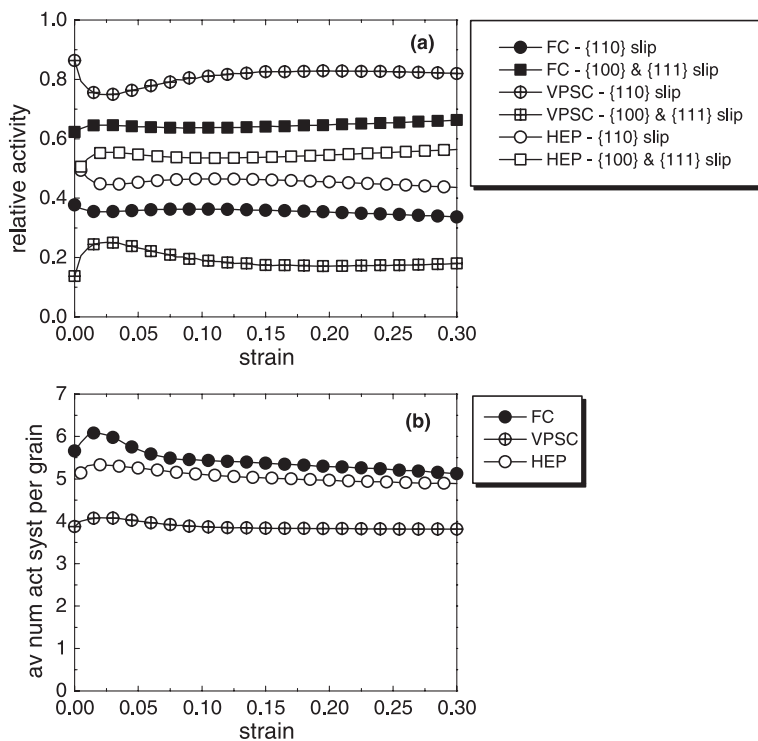


Fig. 12. (a) Relative activity of slip modes and (b) average number of active slip systems per grain predicted with Taylor, VPSC and HEP.

tion: if an arbitrary strain is imposed on a crystal, five independent systems must be activated (the actual number may be higher). Therefore, since there are only two independent variants of the weaker {110} systems, the stronger systems operate profusely. Correspondingly, the average number of active slip systems assumes values between 5.5 and 6. In the VPSC case the weaker {110} system dominates, with only a minor contribution from the stronger systems. In most of the grains, the strain has been accommodated by weaker systems only, leading to high dispersion of the local strain-rate components. Consequently, in the VPSC case, the predicted average number of active slip systems is lower than the Taylor case (approximately 4). The HEP model predicts an intermediate behavior: it gives equal activity for weaker and stronger slip systems at the first deformation step. Then, as deformation proceeds, activity of the stronger systems dominates over that of the weaker systems. This is a consequence of the crystal lattice rotating into harder orientations and to proportionally greater

hardening of the initially weaker {110} systems as deformation proceeds. The average number of active slip systems also is intermediate, closer to Taylor than to VPSC.

5.2. Comparisons to experimental crystallographic textures

Figs. 13 and 14 show inverse pole figures (for 10%, 15% and 30% deformation) obtained with the Taylor, VPSC and HEP models for the 100 and 20 °C cases, respectively. Comparing the simulated 15% strain textures with the experimental textures shown in Fig. 6b (LTA) and c (HTA), we observe that:

(a) At both temperatures, the Taylor model shows at 30% strain a concentration at (111) with a shoulder towards (001) which is the same as the first application of the Taylor theory to halite (Siemes, 1974) and the simulations of Wenk et al. (1989) (see Fig. 1), but contradictory with the experimental results.

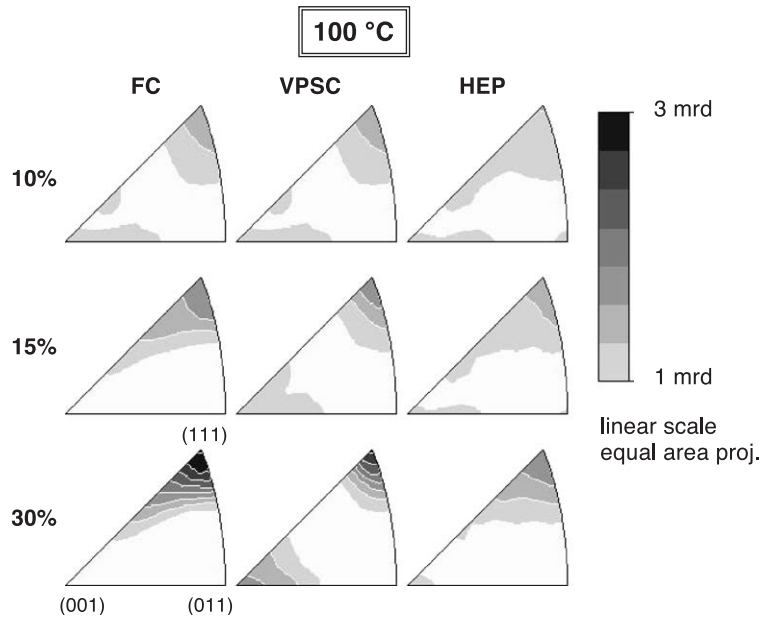


Fig. 13. Inverse pole figures illustrating simulated texture development in halite for 100 °C conditions after 10%, 15% and 30% strain in axial extension obtained with Taylor, VPSC and HEP models. Equal area projection, linear scale contours.

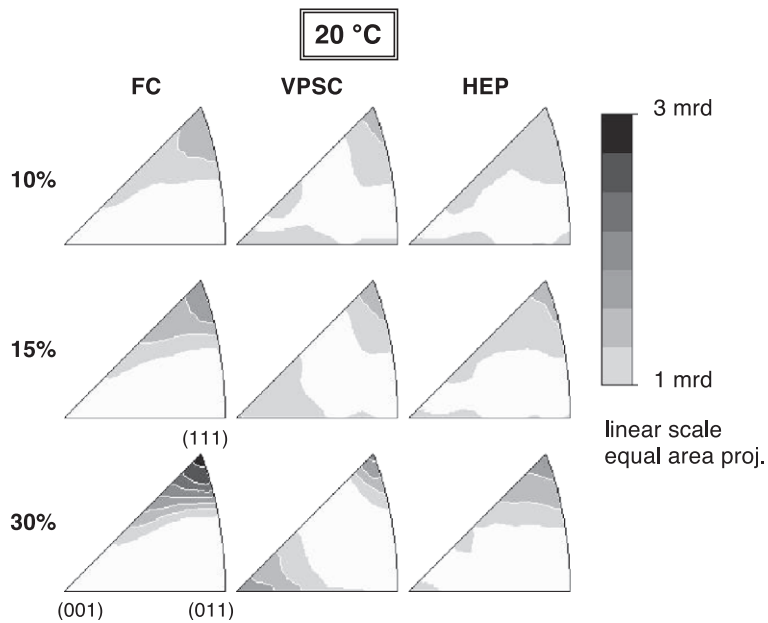


Fig. 14. Inverse pole figures illustrating simulated texture development in halite for 20 °C conditions after 10%, 15% and 30% strain in axial extension obtained with Taylor, VPSC and HEP models. Equal area projection, linear scale contours.

(b) Except for the Taylor model, all the other approaches predict the experimentally observed bimodal (111)–(001) peak distribution, with a dominant (111) component and a secondary component at (001). The (001) component is much stronger for VPSC than for the HEP. Also, the VPSC approach exhibits the two components more distinctly, whereas the HEP displays a characteristic shoulder from (111) towards (001), as observed in experiments.

(c) The general patterns of the VPSC and HEP simulations are similar to earlier VPSC simulations by Wenk et al. (1989) for conditions with significant hardening, but are different from the earlier results for the case with no hardening, shown in Fig. 1.

(d) At 15% strain, the predicted peak intensities are similar to the measured ones, yet a bit sharper in the experimental textures. This contradicts most of our previous experience about comparisons between theoretical and measured textures. In other materials, predicted textures usually are sharper than corresponding measured textures (Kocks et al., 1998).

(e) At 15% strain, the predicted textures at low temperature and at high temperature reach the same peak values. This indicates that both models, HEP and VPSC, are rather insensitive to moderate variations of the single crystal anisotropy and, therefore, that both models fail to predict the measured slight decrease of peak intensities with higher temperature. The reason for this may be that, after all, some amount of recrystallization may have occurred in the experiment, which softened the texture intensity at high temperature. This cannot be predicted without including the effects of recrystallization (which is not currently part of any of the approaches used in this work).

(f) The texture evolution is strongest for the Taylor model, weakest for HEP, and intermediate for VPSC. A reason for this is that both Taylor and VPSC have associated unique reorientation velocities. By contrast, two crystals in the HEP may have different reorientation directions even though they have the same orientation. This gives rise to a variability in the deformation rate predicted with FEM, both in the direction of straining as well as in its magnitude. This variability is a fairly random deviation from the mean which, in turn, gives rise to slower rates of texture evolution.

6. Discussion

6.1. Differences between predicted textures

The Taylor model predicts a texture with a single maximum in (111) that is in disagreement with experiments. As already pointed out by Wenk et al. (1989), crystals with their $\langle 111 \rangle$ direction aligned with the tensile direction are hard and stable orientations. In other words, under Taylor assumptions almost every grain, even those in soft regions near (001), rotates toward this orientation and no further rotation takes place thereafter. In the VPSC results, and less markedly in those of the HEP, a bimodal texture, with a (111) and a (100) component, is formed. In both cases the (111) maximum is stronger than the (100) one, which is in fair agreement with the X-ray textures. The fundamental region of the orientation space for tensile deformation can be divided into two domains. Each domain contains orientations that rotate towards the stable orientations (111) and (001), respectively. The precise limit between both domains depends on the difference in critical shear strengths between the stronger and weaker slip systems. The (111) domain increases in size if the difference between the strength of the weaker and the stronger systems decreases and the behavior predicted by the polycrystal model is closer to compatibility. Consequently, the (001) domain increases if $\{110\}$ is predominantly active and the model is closer to the lower bound. The Taylor model (full compatibility) is an extreme case in which the (111) domain covers the whole orientation space.

This argument suggests that the use of anisotropic hardening laws (i.e. those that change the relative strengths of the weaker and stronger systems with deformation) can change the relative size of both domains, and thus the textures, as deformation proceeds.

6.2. Weakening of theoretical textures

As discussed in the preceding section, the predicted textures are slightly weaker than the experimental textures, in contradiction with our experience in most other materials. A possible explanation for this anomalous behavior of halite is that in the soft $\{110\}$ slip mode, there is, for each individual system (110) $[1\bar{1}0]$,

an equivalent system ($1\bar{1}0$ [110] (slip plane and slip direction exchanged) (Kocks et al., 1998). Both have exactly the same Schmid factor and therefore the same activity. The shears on these systems compensate each other's spins and no texture should develop due to this pair of slip systems, which is one of the reasons why texture evolution is rather weak for the VPSC where $\{110\}$ is dominantly active (see relative activities, Fig. 12). Therefore, grain rotations are mostly due to activation of secondary systems such as $\{111\}$ and

$\{100\}$. There is also a contribution to grain reorientation of rotations associated with changes in grain shape but, for the moderate strains considered in this work, these are small compared with the lattice rotations due to slip activity.

6.3. Comparisons to experimental morphologic textures

Textural data are not the only criterion to compare experiments and simulations. It was noted that predicted strain rates for the three models considered in this paper vary greatly from uniformity in the case of Taylor, a very large orientation dependence in the case of VPSC, and an intermediate pattern for HEP (Fig. 10). Since in the models strain rates are known for each grain and the whole deformation process, we can integrate to obtain the grain shape distribution at any point in the deformation history. Fig. 15 shows a histogram of aspect ratios for VPSC and HEP simulations after 15% strain, for the 100 °C case. This can be compared directly with the experimental data illustrated in Fig. 5. We note that VPSC displays a similar spread as that observed, while predicted grain shapes for HEP are more uniform. It should be emphasized that in the simulations spherical grains were assumed as starting morphology and aspect ratios are for longest versus shortest axis, while in the experiment there was an initial shape distribution and aspect ratios were measured in a section, relative to macroscopic strain coordinates. This would add more spread to the simulated distributions.

7. Conclusions

Even though halite is an extremely simple ionic structure with well-defined slip systems, the mechanical behavior of the polycrystal is rather complicated. Microstructures indicate that deformation is quite heterogeneous, i.e. differently oriented grains deform by different amounts. Thus the classical Taylor theory is not well suited to such a system. We have modeled the deformation of polycrystalline halite with self-consistent (VPSC) and finite element (HEP) approaches, starting from the same initial set of orientations. In both cases, we obtained an average

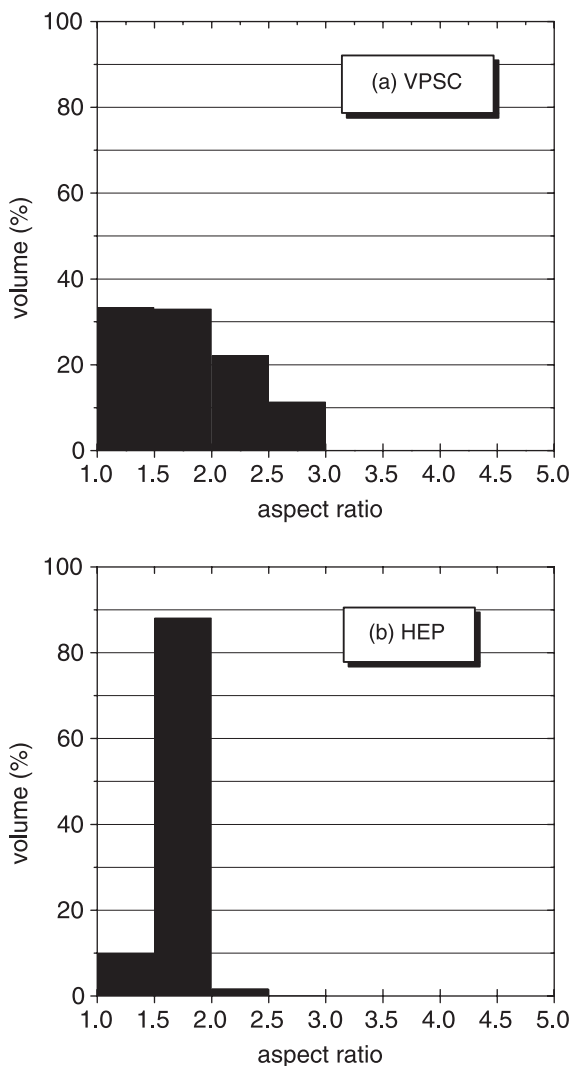


Fig. 15. Aspect ratio distribution after 15% strain predicted with (a) VPSC and (b) HEP models, for the 100 °C case.

deformation for each orientation, but the amount and mode of strain varies from orientation to orientation. In the HEP model, a grain is constrained to have compatibility with neighbors; in the VPSC model, an orientation is constrained only by the average medium. The strain distribution plots (Figs. 10 and 15) point to greater variation that can be captured with finite element simulations only if greater resolution is available, with intragranular heterogeneity. Another large difference is the activity of slip systems. The VPSC formulation concentrates most of the deformation on the weaker system, while in HEP it is more evenly distributed among all systems.

The new polycrystal plasticity simulations of halite highlight significant differences between models that have been routinely applied. The HEP simulations help us to analyze differences between equilibrium and compatibility models. In comparing the VPSC and HEP approaches, the predicted texture development is similar, and therefore not a good criterion to discriminate between them. Predicted microstructures show greater differences, and at least qualitatively, the similar and low aspect ratios observed in the experiments are more compatible with the VPSC predictions. While the VPSC spread looks better in comparison to the data (Fig. 3), that is somewhat misleading. The experiments show very little increase in volume fraction of grains with aspect ratio above 2.5. The fact that VPSC has a large fraction above 2.5 probably relates back to the high D_{33} values in Fig. 10a and is not very realistic. The HEP model, on the other hand, seems to constrain the deformation too much, probably due to the simple representations of the crystals. We have illustrated that, with a model like HEP, which captures more of the physics of polycrystal deformation by imposing equilibrium and compatibility at the local scale, the evolution of texture as well as of microstructure, are adequately predicted. This comes at the cost of added complexity.

Also the HEP formulation and the microstructure considered here are still highly idealized. Microstructural observations on highly deformed plastically anisotropic minerals and rocks indicate pervasive heterogeneous deformation within a crystal. We consider this study as an intermediate step to advance to a more realistic polycrystal in which domains within a crystal can deform differently. Finite element simulations in which many elements cover a crystal have

been done for cubic metals with a single slip system (Mika and Dawson, 1999), and it is planned to extend them to halite and at that stage explore local differences between grains in more detail. In the future much attention must be paid to local features such as grain shape, slip system activity, dislocation distributions to determine the quality of a model and estimate the extent to which it is applicable.

Acknowledgements

HRW is grateful for support through IGPP-LANL, NSF (EAR 99-02866), Humboldt foundation during a research leave at the Bayerisches Geoinstitut in Bayreuth, where this paper was completed. HMK is grateful to T. Popp and D. Schulte-Kortnack for their help in performing the experiments and to G. Braun for doing the X-ray texture measurements.

References

- Barton, N.R., Dawson, P.R., 2001. On the spatial variations in orientations and misorientations in two phase titanium. *Mod. Sim. Mater. Sci. Eng.* 9, 433–463.
- Beaudoin, A.J., Dawson, P.R., Mathur, K.K., Kocks, U.F., 1995. A hybrid finite element formulation for polycrystal plasticity with consideration of macrostructural and microstructural linking. *Int. J. Plast.* 11, 501–521.
- Canova, G.R., Kocks, U.F., Jonas, J.J., 1984. Theory of torsion texture development. *Acta Metall.* 32, 211–226.
- Carter, N.L., Heard, H.C., 1970. Temperature and rate-dependent deformation of halite. *Am. J. Sci.* 269, 193–249.
- Carter, N.L., Horseman, S.T., Russel, J.E., Handin, J., 1993. Rheology of rocksalt. *J. Struct. Geol.* 15, 1257–1271.
- Dawson, P.R., Beaudoin, A.J., Mathur, K.K., Sarma, G.B., 1994. Finite element modeling of polycrystalline solids. *Eur. J. Finite Elem.* 3, 543–571.
- Franssen, R.C.M.W., 1996. Mechanical anisotropy of synthetic polycrystalline rocksalt. In: Aubertin, M., Hardy, H.R. (Eds.), *Proc. 4th. Conf. on the Mechanical Behavior of Salt*, pp. 101–114.
- Franssen, R.C.M.W., Spiers, C.J., 1990. Deformation of polycrystalline salt in shear at 250–350 °C. In: Knipe, R.J., Rutter, E.H. (Eds.), *Deformation Mechanisms. Rheology and Tectonics. Geol. Soc. London, Spec. Publ.*, vol. 45, pp. 201–213.
- Guillope, M., Poirier, J.-P., 1979. Dynamic recrystallization during creep of single-crystalline halite: an experimental study. *J. Geophys. Res.* 84, 5557–5567.
- Heard, H.C., 1972. Steady state flow in polycrystalline halite at a pressure of two kilobars. In: Heard, H.C., et al. *Flow and Fracture of Rocks. Am. Geophys. U. Monogr.*, vol. 16, pp. 191–209.
- Hughes, D.A., Lebensohn, R.A., Wenk, H.-R., Kumar, A., 2000.

- Stacking fault energy and microstructure effects on torsion texture evolution. *Proc. R. Soc. Lond.*, A 456, 1–33.
- Kern, H.M., 1979. Texture development in calcite and quartz deformed at uniaxial and real triaxial states of strain. *Bull. Mineral.* 102, 290–300.
- Kern, H.M., Braun, G., 1973. Deformation und Gefügeregelung von Steinsalz im Temperaturbereich 20–200 °C. *Contrib. Mineral. Petrol.* 40, 169–181.
- Kocks, U.F., Tomé, C.N., Wenk, H.-R., 1998. Texture and Anisotropy. Preferred Orientations in Polycrystals and Their Effect on Materials Properties. Cambridge Univ. Press, Cambridge.
- Lebensohn, R.A., Tomé, C.N., 1993. A self-consistent approach for the simulation of plastic deformation and texture development of polycrystals: application to zirconium alloys. *Acta Metall. Mater.* 41, 2611–2624.
- Lebensohn, R.A., Tomé, C.N., 1994. A self-consistent visco-plastic model: calculation of rolling textures of anisotropic materials. *Mater. Sci. Eng. A* 175, 71–82.
- Lequeu, P., Gilormini, P., Montheillet, F., Bacroix, B., Jonas, J.J., 1987. Yield surfaces for textured polycrystals: I. Crystallographic approach. *Acta Metall.* 35, 439–451.
- Masson, R., Bornert, M., Suquet, P., Zaoui, A., 2000. An affine formulation for the prediction of the effective properties of nonlinear composites and polycrystals. *J. Mech. Phys. Solids* 48, 1203–1227.
- Mecking, H., Kocks, U.F., Hartig, C., 1996. Taylor factors in materials with many deformation modes. *Scr. Mater.* 35, 465–471.
- Mika, D.P., Dawson, P.R., 1999. Polycrystal plasticity modeling of intracrystalline boundary textures. *Acta Mater.* 47, 1355–1369.
- Molinari, A., Canova, G.R., Ahzi, S., 1987. A self-consistent approach of the large deformation polycrystal viscoplasticity. *Acta Metall.* 35, 2983–2994.
- Ponte Castañeda, P., 1991. The effective mechanical properties of nonlinear isotropic composites. *J. Mech. Phys. Solids* 39, 45–71.
- Ponte Castañeda, P., 1996. Exact second-order estimates for the effective mechanical properties of non-linear composite materials. *J. Mech. Phys. Solids* 44, 827–862.
- Sannemann, D., 1968. Salt-stock families in northwestern Germany. In: Braunstein, J., O'Brian, G.D. (Eds.), *Diapirism and Diapirs Symposium. Mem. Amer. Assoc., Petroleum Geologists*, vol. 8, pp. 261–270. Tulsa, Oklahoma.
- Sarma, G.B., Dawson, P.R., 1996. Effects of interactions among crystals on the inhomogeneous deformations of polycrystals. *Acta Mater.* 44, 1937–1953.
- Siemes, H., 1974. Anwendung der Taylor Theorie auf die Regelung von kubischen Mineralen. *Contrib. Mineral. Petrol.* 43, 149–157.
- Skrotzki, W., Haasen, P., 1981. Hardening mechanisms of ionic crystals on {110} and {100} slip planes. *J. Physique* 42 (C3), 119–148.
- Skrotzki, W., Welch, P., 1983. Development of texture and microstructure in extruded ionic polycrystalline aggregates. *Tectonophysics* 99, 47–62.
- Skrotzki, W., Helming, K., Brokmeier, H.-G., Dornbusch, H.-J., Welch, P., 1995. Textures in pure shear deformed rock salt. *Textures Microstruct.* 24, 133–141.
- Skrotzki, W., Dornbusch, H.-J., Helming, K., Tamm, R., Brockmeier, H.-G., 1996. Development of microstructure and texture in pure shear deformed salt. In: Aubertin, M., Hardy, H.R. (Eds.), *Proc. 4th. Conf. on the Mechanical Behavior of Salt*, pp. 203–211.
- Skrotzki, W., Tamm, R., Oertel, C.-G., Röseberg, J., Brokmeier, H.-G., 2000. Microstructure and texture formation in extruded lead sulfide (galena). *J. Struct. Geol.* 22, 1621–1632.
- Taylor, G.I., 1938. Plastic strain in metals. *J. Inst. Met.* 62, 307–324.
- Tomé, C.N., Canova, G.R., 1998. Self-consistent modeling of heterogeneous plasticity. In: Kocks, U.F., Wenk, H.-R. (Eds.), *Texture and Anisotropy*. Cambridge University Press, Cambridge, pp. 466–511. Chapter 11.
- Tomé, C.N., Kocks, U.F., 1985. The yield surface of hcp crystals. *Acta Metall.* 33, 603–621.
- Trimby, P.W., Drury, M.R., Spiers, C.J., 2000. Misorientations across etched boundaries in deformed rocksalt: a study using electron backscatter diffraction. *J. Struct. Geol.* 22, 81–89.
- Trusheim, F., 1957. Über Halokinese und ihre Bedeutung für die strukturelle Entwicklung Norddeutschlands. *Z. Dtsch. Geol. Ges.* 109, 11–151.
- Trusheim, F., 1960. Mechanisms of salt migration in northern Germany. *Bull. Am. Assoc. Petrol. Geol.* 44, 1519–1540.
- Van Houtte, P., 1982. On the equivalence of the relaxed Taylor theory and the Bishop–Hill theory for partially constrained plastic deformation of crystals. *Mater. Sci. Eng.* 55, 69–77.
- Wenk, H.-R., 1999. A voyage through the deformed Earth with the self-consistent model. *Mod. Sim. Mater. Sci. Eng.* 7, 699–722.
- Wenk, H.R., Canova, G.R., Molinari, A., Mecking, H., 1989. Texture development in halite: comparison of Taylor model and self-consistent theory. *Acta Metall.* 37, 2017–2029.
- Wenk, H.-R., Canova, G.R., Brechet, Y., Flandin, L., 1997. A deformation-based model for recrystallization of anisotropic materials. *Acta Mater.* 45, 3283–3300.
- Wenk, H.-R., Matthies, S., Donovan, J., Chateigner, D., 1998. BEARTEX, a Windows-based program system for quantitative texture analysis. *J. Appl. Crystallogr.* 31, 262–269.
- Zienkiewicz, O.Z., Taylor, R.L., 2000. *The Finite Element Method: Volume I. The Basis*, 5th ed. Butterworth-Heinemann, Oxford. Chap. 13.